ROYAL SOCIETY OF CHEMISTRY

Check for updates

High-efficiency TADF materials featuring carbazole-modified spiroacridan-pyrimidine skeletons with an external quantum efficiency exceeding 26% in sky-blue light emission†

Yi-Zhen Li, ‡[a] Fu-En Szu, ‡[a] Han-Yun Szu,[a] Chao-Che Wu,[b] Yong-Yun Zhang,[a] Zong-Huan Li,[a] Jiun-Haw Lee, *[b] Tien-Lung Chiu *[c] and Man-kit Leung *[ad]

We report the design and synthesis of a novel sky-blue TADF emitter, **4SpAc35CzPy**, incorporating spiroacridan as the donor and pyrimidine as the acceptor. Compared to the previously reported **4Ac35CzPy** emitter, incorporating the fluorenyl group controlled the twisting angle of the spiroacridan structure, enhancing the ICT (intramolecular charge transfer) effect and improving TADF performance. Introducing the spirofluorenyl group to the acridan suppresses energy loss caused by intramolecular vibrations, further optimizing the TADF characteristics. The electroluminescent device with a light emitting layer of 3% **4SpAc35CzPy** doping concentration in **o-DiCbzBz** falls within the sky-blue light range, exhibiting an emission λ_{max} of 480 nm at 9.5 V with a CIE of (0.165,0.274) and a brightness of 1677 cd m^{-2}. An external quantum efficiency (η_{EQE}) of 20.2%, a current efficiency (η_{CE}) of 36.9 cd A^{-1}, and a power efficiency (η_{PE}) of 33.2 lm W^{-1} were achieved. Adjusting the doping concentration leads to an even more efficient device with an η_{EQE} of 26.7%, an η_{CE} of 55.7 cd A^{-1}, and an η_{PE} of 50.1 lm W^{-1}, outperforming similar acridan-based compounds. Natural orbital analysis reveals that the high TADF-OLED performance of **4SpAc35CzPy** may be attributed to the multichannel high-lying reverse intersystem crossing of the hot triplet excitons back to their S$_2$ and S$_3$ states for luminescence.

[a] *Department of Chemistry, National Taiwan University, Taipei, 10617, Taiwan.*
  E-mail: mkleung@ntu.edu.tw
[b] *Graduate Institute of Photonics and Optoelectronics and Department of Electrical Engineering, National Taiwan University, Taipei, 10617, Taiwan.*
  E-mail: jiunhawlee@ntu.edu.tw
[c] *Department of Electrical Engineering, Yuan Ze University, Chung-Li, Taoyuan, 32003, Taiwan. E-mail: tlchiu@saturn.yzu.edu.tw*
[d] *Advanced Research Center for Green Materials Science and Technology, National Taiwan University, Taipei, 10617, Taiwan*

‡ Yi-Zhen Li and Fu-En Szu contributed equally to this work.

Introduction

In OLED technology, the thermally activated delayed fluorescence (TADF) mechanism has been extensively utilized over decades.[1–4] It harnesses 25% of singlet excitons and effectively utilizes the remaining 75% of triplet excitons[5] for fluorescence. By employing the reverse intersystem crossing (rISC) mechanisms, the triplet excitons turn back to the singlet S$_1$ state for delayed fluorescence emission, making an internal quantum efficiency (IQE) of 100% possible.[6–9] Moreover, the TADF emitters are usually fully organic; precious heavy metal ions are no longer indispensable. Effective molecular design further allows for fine-tuning of the emission colour, and the singlet–triplet energy (ΔE_{ST}) splitting to enhance the TADF efficiency.[10–12]

TADF molecules are usually bipolar; matching the electron-donating groups (donors) with electron-withdrawing groups (acceptors) not only determines the emission colour but also leads to spatial separation of the highest occupied molecular orbital (HOMO) and the lowest unoccupied molecular orbital (LUMO), beneficial for the rISC process and the TADF properties.[13–15] Common donors include acridan,[16,17] phenoxazine,[18,19] and phenothiazine.[20] Spiroacridan, in particular, has been extensively used as a donor, capitalizing on its strong electron-donating capabilities.[21–24] Additionally, the molecular rigidity of spiroacridan enhances the material's thermal stability and usually leads to superior device performance compared to 9,9-dimethylacridine.[25,26]

As an electron acceptor, pyrimidine-based OLEDs can be broadly categorized into two configurations of D–A and D–A–D.[27–32] The D–A–D configuration is more commonly used due to its higher external quantum efficiency (η_{EQE}) compared to

This journal is © The Royal Society of Chemistry 2025
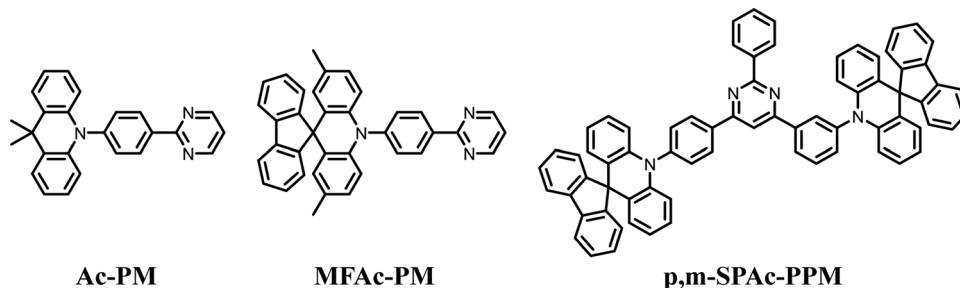
J. Mater. Chem. C, 2025, 13, 14527–14538 | **14527**

Fig. 1   The molecular structures of pyrimidine derivatives.[26,28]

the D–A system.[15,29,33] However, this often results in a redshift in the emission spectrum, potentially extending from blue-green to green light. Therefore, we adopted a more challenging D–A system to study; emission within the blue to sky-blue colour range and high efficiency are two challenging goals for us to achieve.

Yasuda reported a series of D–A type pyrimidine TADF materials featuring different donors linked at the 2-position of the pyrimidine group, which are presented in Fig. 1.[26] Among these, in MFAc-PM and Ac-PM, it is evident that although the emission colour of MFAc-PM is slightly red-shifted, there is a significant improvement in its η_{EQE}, current efficiency (η_{CE}), and power efficiency (η_{PE}). Specifically, MFAc-PM achieves a maximum η_{EQE} of 17.1%, an η_{CE} of 34.3 cd A^{-1}, and an η_{PE} of 31.7 lm W^{-1}, which are considerably better than Ac-PM's maximum η_{EQE} of 11.4%, η_{CE} of 18.9 cd A^{-1}, and η_{PE} of 16.5 lm W^{-1}. Recently, p,m-SPAc-PPM, a novel creation featuring two spiroacridan groups strategically placed at the 4 and 6 positions, has been synthesized. Again, this asymmetric D–A–D type TADF material still captured an impressive η_{EQE} of 25.1%, radiating a peak emission at 486 nm.[28] Relevant data on recent sky-blue OLED materials are also included in the ESI† (Table S6).[28,34–42]

In our previous research, we attempted to examine if the D–A type design could reach a similar level of η_{EQE}. Our design is also shown in Fig. 2, using an acridan–pyrimidine framework. Compounds like 4Ac25CzPy and 4Ac35CzPy, equipped with a 9,9-dimethylacridine group as an electron-donating group on the pyrimidine system, exhibited emission colours in sky blue and blue-green with the maximum η_{EQE} of 12.4% and 21.2%, respectively.[42] These were achieved by strategically placing carbazole groups at different positions to fine-tune the

HOMO levels, emission colours, and steric environment properties.

Since the 3,5-dicarbazolyl derivative 4Ac35CzPy shows a higher η_{EQE} in the previous study, we replace the 9,9-dimethyl-acridine group with a rigid spiroacridan group to give 4SpAc35CzPy, a new TADF emitter in the present study. Desired sky-blue materials with an η_{EQE} of 26.7%, an η_{CE} of 55.7 cd A^{-1}, and an η_{PE} of 50.1 lm W^{-1} have been recorded.

Results and discussion

Materials and methods

Synthesis of 4SpAc35CzPy: to a mixture of 2,4,5-trifluoro-phenylboronic acid (1.5 eq.), 2-bromopyrimidine (1 eq.), Pd(OAc)$_2$ (5 mol%), and triphenylphosphine (20 mol%) under argon were added dimethoxyethane (DME, 1 M) and K$_2$CO$_{3(aq)}$ (2.7 M, 2.6 eq.) respectively. The mixture was refluxed at 105 °C for 2.5 h to afford 1 (70%). A mixture of 1 (1.08 eq.), 10H-spiro[acridine-9,9′-fluorene] (1 eq.), and Cs$_2$CO$_3$ (1.5 eq.) in DMSO (1 M) was then refluxed at 200 °C under argon for 15 h to give 2 (65%). Finally 2 (1 eq.), carbazole (1.2 eq.), and Cs$_2$CO$_3$ (1.5 eq.) in DMSO (1 M) were reacted at 200 °C under argon for 15 h to provide 4SpAc35CzPy (73%). The structural character-isation of 4SpAc35CzPy is reported in pages S2–S7 (ESI†).

Absorption and luminescence spectra were recorded using an ultraviolet-visible (UV-vis) absorption spectrometer (Hitachi U-4100 UV-vis-NIR) and photoluminescence (PL) spectrometer (Hitachi F-4500). Time-resolved photoluminescence (TrPL) measurements for the exciton dynamics of the materials were carried out using second-harmonic generation from a femtose-cond Ti:sapphire pulse laser and a fast time-resolved streak camera (Hamamatsu C4334, 15 ps resolution). The photolumi-nescence quantum yield (PLQY) was measured with a setup of a xenon lamp and monochromator (Horiba iHR320), an integrat-ing sphere (Quanta-φ manual Rev C F-3029), a photomultiplier tube (PMT, Hamamatsu), and the FluorEssence software pack-age. Thin-film OLEDs were fabricated by thermal evaporation of the materials onto indium-tin-oxide (ITO) substrates with a sheet resistance of 30 Ω sq^{-1}, serving as the transparent anode. The ITO plates were cleaned in an ultrasonic bath, using acetone, isopropanol, and deionized water as cleansers, fol-lowed by O$_2$ plasma treatment before use. Organic and metal layers were deposited under high vacuum conditions (<10^{-6} Torr). Device encapsulation was performed in a
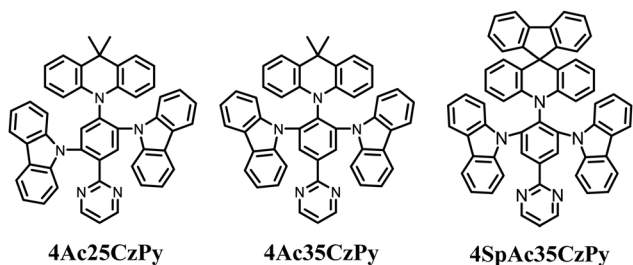

Fig. 2   Structural formulas of 4Ac25CzPy, 4Ac35CzPy, and 4SpAc35CzPy.[42]

nitrogen-filled glovebox ($O_2 < 0.1$ ppm, $H_2O < 0.1$ ppm). The active area of the OLEDs was 2×2 mm². Electroluminescence (EL) characterization was conducted using a source meter (Keithley 2400) and a spectrometer (Minolta CS-1000). Time-resolved electroluminescence (TrEL) measurements were performed using a waveform function generator (Agilent 335011B) to drive the devices, a photomultiplier tube (Hamamatsu H6780-20), and an oscilloscope (Tektronix TSB2202B) to detect and record the emitted optical signals.

To understand the TADF behaviour of **4SpAc35CzPy**, we evaluated the interactions between the donor and acceptor components using density functional theory (DFT). To compare the properties of **4Ac35CzPy** and **4SpAc35CzPy**, calculations for **4Ac35CzPy** were also performed at the same level based on the X-ray geometry. Molecular orbital calculations were performed based on the X-ray geometry using Gaussian 16 at the DFT/B3LYP-D3BJ/Def2TZVP level.[43] Natural transition orbital (NTO) analyses were also performed, using the TDDFT/B3LYP-D3BJ functional with the def-TZVP basis set. However, the solvent parameter of 2-methyltetrahydrofuran (2-MeTHF) was selected to simulate the dielectric environment in solid films during spectroscopic measurements. Spin–orbit coupling (SOC) matrix elements between the singlet excited states (S_n, for $n = 0–4$) and triplet excited states (T_n, for $n = 1–10$) were calculated using the ORCA software package.

Synthesis of 4SpAc35CzPy

The synthesis route for **4SpAc35CzPy** is shown in Scheme 1, and the procedures are described in the ESI.† The Suzuki–Miyaura cross-coupling reaction with 2-bromopyrimidine and 3,4,5-trifluorophenylboronic acid gave **1**[42] that was subsequently reacted with 10H-spiro[acridine-9,9'-fluorene] (SpAc), followed by two equivalents of carbazole through nucleophilic aromatic substitution (S_NAr) to afford the desired product **4SpAc35CzPy**. In the S_NAr substitutions, the 4-fluoro substituent is relatively more reactive than those at 3 and 5 positions; the SpAc group could, therefore, be introduced selectively to the 4-position in the first S_NAr step. **4SpAc35CzPy** was purified by sublimation under reduced pressure ($< 1 \times 10^{-5}$ Torr) and identified by ¹H, ¹³C, and ¹⁹F NMR spectroscopy (Fig. S1–S5, ESI†), high-resolution mass spectrometry (HRMS) and single-crystal X-ray diffraction (XRD).
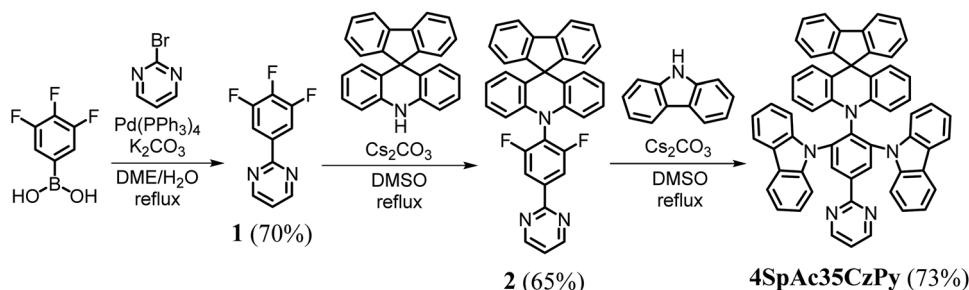
Crystallographic analysis

X-ray crystallographic structural analysis of **4SpAc35CzPy** is presented in Fig. 3a and b and compared against **4Ac35CzPy** in Fig. 3c and d, providing insights into the molecular conformation. The dihedral angle between the central benzene ring and the SpAc moiety is 71.1° (68.2°), larger than the dihedral angle of 70.0° (65.4°) of **4Ac35CzPy**. Presumably attributable to the rigidity of SpAc and the symmetrical 1,2,3-ortho-substituent arrangement, the middle SpAc moiety may experience the same repulsions from carbazoles on both sides. The conformation of the central six-membered ring of **4SpAc35CzPy** is relatively co-planar compared to the slightly pyramidal conformation at the nitrogen atom of **4Ac35CzPy**. On the other hand, the dihedral angle between the benzene and the pyrimidine is 28.0°, which is smaller than the dihedral angle of 30.0° of **4Ac35CzPy**, implying a similar ΔE_{ST} and TADF emission characteristics.

Density functional theory calculations. The key Frontier molecular orbitals of **4Ac35CzPy** and **4SpAc35CzPy**, including the HOMO−1, HOMO, LUMO, and LUMO+1, along with their corresponding energy levels, are summarized in Table 1.

4SpAc35CzPy and **4Ac35CzPy** exhibited similar results, which can be categorized into distinct donor and acceptor regions: (1) the electron-donating spiroacridan or carbazole units and (2) the electron-accepting central benzene ring and pyrimidine core. The spiroacridan fragments primarily contribute to the HOMO, while the HOMO−1 is predominantly from the carbazole fragments. On the other hand, the LUMO and LUMO+1 orbitals arise from the central benzene ring associated with the pyrimidine core. Although the HOMO and LUMO orbitals are spatially separated, the two regions still interact through the phenylene bridge, consistent with the observed TADF photophysical properties and a reasonable photoluminescence quantum yield.

The fluorescence emission from the S_1 to S_0 transition of both materials primarily originates from the HOMO to LUMO transition. The emission wavelength calculated for **4SpAc35CzPy** is 434 nm, while for **4Ac35CzPy** is 441 nm. Based on these results, it can be inferred that the emission colour of **4SpAc35CzPy** is slightly blue-shifted compared to that of **4Ac35CzPy**.

Thermal properties. **4SpAc35CzPy** exhibits a high thermal 5% weight loss temperature (T_d) of 407 °C in the thermogravimetric

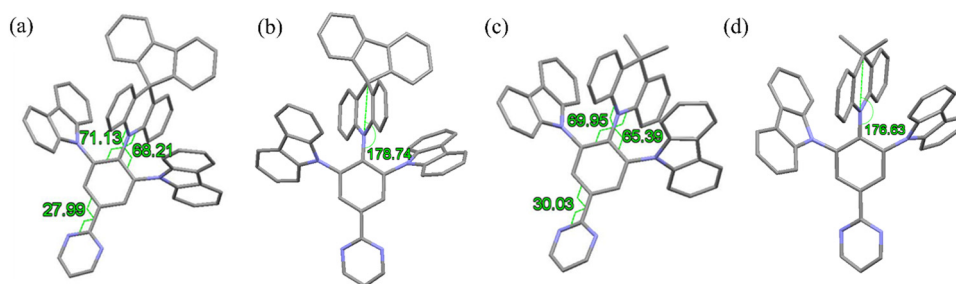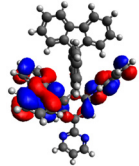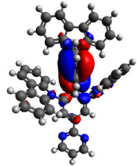**Scheme 1** Synthetic route and the molecular structure of **4SpAc35CzPy**.
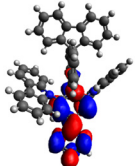
This journal is © The Royal Society of Chemistry 2025

J. Mater. Chem. C, 2025, **13**, 14527–14538 | **14529**
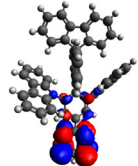
Fig. 3 Comparison of the X-ray crystallographic structures of **4SpAc35CzPy** (a) and (b) and **4Ac35CzPy** (c) and (d) with capped-stick representations.

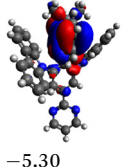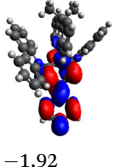**Table 1** Calculated orbitals and the corresponding orbital energies (in eV) of **4SpAc35CzPy** and **4Ac35CzPy** at their respective minimum S_0 structures at the DFT/B3LYP-D3BJ/Def2TZVP level

Species	HOMO−1	HOMO	LUMO	LUMO+1
4SpAc35CzPy	−5.85	−5.46	−2.01	−1.69
4Ac35CzPy	−5.79	−5.30	−1.92	−1.69

analysis (TGA), (Fig. S6, ESI†) compared with **4Ac35CzPy** that has a T_d of 344 °C only. Furthermore, neither a clear-cut glass transition temperature (T_g) nor melting temperature (T_m) was observed below 220 °C in the amorphous state in the second round of DSC scanning. However, an observed small DSC step at 235 °C may be due to the glass transition (Fig. S7, ESI†). In short, **4SpAc35CzPy** shows high thermal stability that may benefit its OLEDs' operational lifetime.

Electrochemical properties. The HOMO energy level of **4SpAc35CzPy** was further estimated by cyclic voltammetry (CV) and differential pulse voltammetry (DPV). The

corresponding redox potentials are summarized in Table 2 and presented in Fig. S8, ESI.† The oxidation scan was measured in dichloromethane, and the reductive scan was performed in N,N-dimethylformamide. The values of $E_{\text{DPV}}^{\text{ox}}$ and $E_{\text{DPV}}^{\text{re}}$ for **4SpAc35CzPy** are 0.65 V and −2.22 V, respectively, when using ferrocene (Fc) as the internal standard. Since the HOMO of −5.23 eV for Fc has been reported,[36] the HOMO and LUMO levels around 5.87 eV and 3.01 eV for **4SpAc35CzPy** are estimated according to the DPV values of the oxidation and the reduction waves, respectively. The HOMO–LUMO energy level alignments well match with those of **o-DiCbzBz**, our OLED

Table 2 Photophysical properties, state, and HOMO/LUMO energy levels of **4SpAc35CzPy**

Material	Absorption [nm] solution/film[a] $\lambda_{\text{onset}}^{\text{abs}}$	E_g [eV][b] solution/film	Emission [nm] solution (77 K[c], rt[a])/film			S_1^d [eV]	T_1^e [eV]	ΔE_{ST}^f [eV]	Φ^g [%]	Energy level [Film (CV), eV] HOMO/LUMO
			$\lambda_{\text{max}}^{\text{FL}}$ [a]	$\lambda_{\text{onset}}^{\text{FL}}$ [j]	$\lambda_{\text{onset}}^{\text{LTPH}}$ [c]					
4SpAc35CzPy	437/438[j]	2.8/2.8	500/500	410, 437/438	450/—	2.83	2.75	0.08	63/62/74	5.8[h] (5.87[i])/3.0[h] (3.01[i])
4Ac35CzPy[k]	436/460	2.8/2.7	480/508	423, 436/460	456/—	2.93	2.72	0.14	70/—/65	5.6[h] (5.47[i])/2.9[h] (2.85[i])

[a] Measured in solution of THF (1 × 10⁻⁵ M) [b] Estimation of the energy gap using equation 1240.8/$\lambda_{\text{onset}}^{\text{abs}}$. [c] Measured in 2-MeTHF with a concentration of 1 × 10⁻⁵ M at 77 K and room temperature. [d] Estimated singlet state energy using equation 1240.8/$\lambda_{\text{onset}}^{\text{FL}}$ in the film state. [e] Estimated triplet state energy using 1240.8/$\lambda_{\text{onset}}^{\text{LTPH}}$ in 2-MeTHF glass at 77 K. [f] ΔE_{ST}. [g] Measured in THF solution, pristine film, and doped in **o-DiCbzBz**. Anthracene was used as a reference in cyclohexane. [h] Value in film: HOMO is measured using an AC-II and LUMO = HOMO − E_g. [i] F$_C$ (HOMO) = −5.23 eV.[44] [j] Estimated from the crossover point of CT absorption and fluorescence spectra. The CT absorption of **4SpAc35CzPy** in the film state is unclear. However, the photoluminescence (PL) emission spectrum is almost identical to the solution PL spectrum. The same onset is, therefore, assigned. [k] See ref. 42.

14530 | *J. Mater. Chem. C*, 2025, **13**, 14527–14538

This journal is © The Royal Society of Chemistry 2025

host. The higher HOMO with a lower LUMO level for **4SpAc35CzPy** *versus* **o-DiCbzBz** implies that it should have more substantial electron donating and better electron accepting characteristics in **o-DiCbzBz**. These are consistent with our previous results in X-ray crystallographic analysis and our theoretical studies.

Photophysical properties. The photophysical properties, including UV-vis absorption and photoluminescence spectra of **4SpAc35CzPy** in the solution, are shown in Fig. 4a, and the parameters are summarized in Table 2. UV-vis absorption was measured in THF solution under ambient conditions, and low-temperature fluorescence (LTFL) and low-temperature phosphorescence (LTPh) were measured in 2-methyltetrahydrofuran (2-MeTHF) with a concentration of 1×10^{-5} M at 77 K. 2-MeTHF has been used for measurement to avoid crystallization at low temperatures. Furthermore, the thin-film photoluminescence (PL), presented in Fig. 4b, was also measured to simulate the emission in the device.

The UV-vis absorption spectrum shows strong absorption between 250 and 350 nm, arising from the π–π^* transition of the conjugated aromatic moieties, along with weaker absorption at around 350–450 nm, which is attributed to the intramolecular charge transfer (ICT) transition from the SpAc group through the central benzene ring to the pyrimidine group.

4SpAc35CzPy fluoresces at room temperature with the λ_{max} at 500 nm either in solution or a pristine thin film. The photoluminescence quantum yields are 0.63 and 0.62, respectively. The broad and structureless PL pattern suggests a CT character in the excited state. Perhaps due to the high conformational rigidity of **4SpAc35CzPy**, the extent of conformational relaxation in the excited state is relatively small. Therefore, their photoluminescence (PL) emission spectra in solution and the film state are almost identical. The same fluorescence onset is, therefore, assigned. However, at 77 K, the low-temperature fluorescence (LTFL) spectrum of **4SpAc35CzPy** shows an emission onset at 410 nm and peaks at 440 nm, which is about 60 nm shorter when compared with that at room temperature. A vibronic pattern can be seen in the fluorescence spectrum. The spectral blue shift at 77 K is probably due to the restricted solvent dipole relaxation in

2-MeTHF organic glass; stabilization of the CT excited state through dipole–dipole interactions is prohibited. In this situation, the Frank–Condon excited state becomes the S_1 state, which has a lower energy than the CT excited state (S_2).

The phosphorescence (PH) vibronic spectrum at 77 K shows an onset at 450 nm and has the maximum emission at 471 nm, which overlaps with the fluorescence spectrum at room temperature. Even though the attempts to collect the phosphorescence data of **4SpAc35CzPy** at room temperature were unsuccessful, the estimated ΔE_{ST} at 77 K is about 0.27 eV, which is still smaller than the TADF criteria of 0.3 eV, strongly suggesting the potential of having TADF effects. As the OLEDs operate at room temperature, if one estimates the ΔE_{ST} using the singlet and triplet energies derived from the room-temperature fluorescence onset (λ_{onset}^{FL}) and the low-temperature phosphorescence (λ_{onset}^{LTPH}), respectively, with the λ_{onset}^{FL} of **4SpAc35CzPy** being 438 nm (2.83 eV) and the triplet energy (T_1) being estimated at 2.75 eV from the λ_{onset}^{LTPH}, a very small ΔE_{ST} value of merely 0.08 eV is expected. These results indicate that **4SpAc35CzPy** may show substantial potential as a TADF material.

The TADF behavior of **4SpAc35CzPy** in a pristine thin film has been further evaluated by transient photoluminescence (TrPL) measurements, as shown in Fig. 5 and Table 3. The profile of the photoluminescence (PL) intensity *versus* time for **4SpAc35CzPy**, after a laser pulse excitation, shows a luminescence prompt decay with a half-life in a nano-second time scale of τ_p = 11.3 ns (Fig. 5a), followed by a slow decay half-life in a micro-second time scale of τ_d = 73.2 μs (Fig. 5b). Since the total photoluminescence quantum yield is 62% (Fig. S9(a), ESI†), integration of the prompt and slow decay signals resolved that the prompt decay quantum yield is 38.1%. The slow decay quantum yield is 23.9% (Table 3). The prompt PL decay rate of **4SpAc35CzPy** is similar to or slightly faster than that of **4Ac35CzPy**. On the other hand, the delayed PL decay of **4SpAc35CzPy** is faster than that of **4Ac35CzPy** in the pristine film. Careful examination of their rate constants reveals that the non-radiative decay of **4SpAc35CzPy** is significantly larger. Conversely, the reverse inter-system crossing of **4SpAc35CzPy** is less effective. This is probably due to the intermolecular
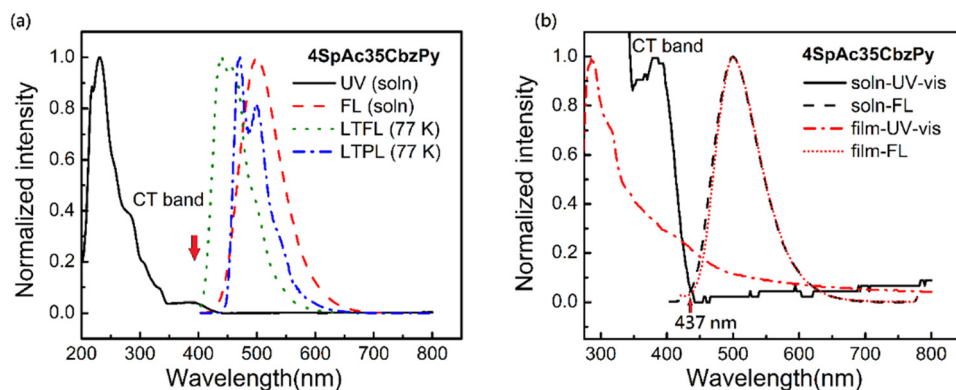

Fig. 4 UV-vis and PL spectra of **4SpAc35CzPy** in (a) solution; (b) thin film (solvent).

This journal is © The Royal Society of Chemistry 2025

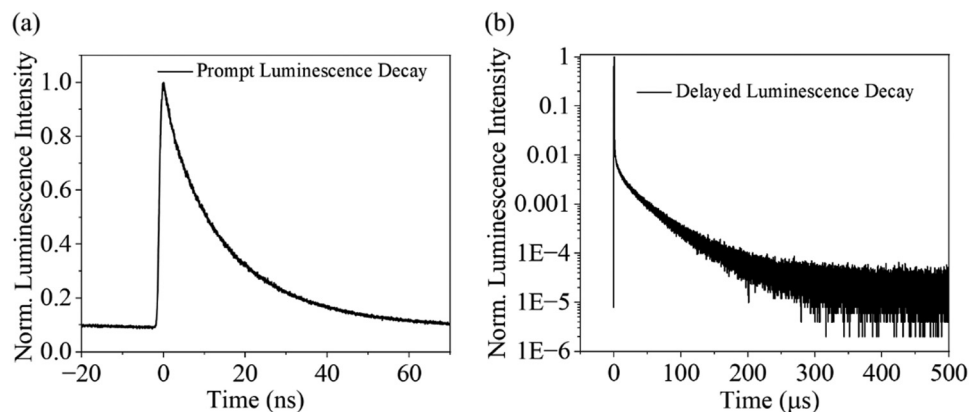*J. Mater. Chem. C*, 2025, **13**, 14527–14538 | **14531**

Fig. 5 TrPL of (a) prompt and (b) delayed decay curves of **4SpAc35CzPy** in the pristine film.

Table 3 Transient photoluminescence data of **4SpAc35CzPy** in the film state

Film	$\Phi_{total}/\Phi_{prompt}/\Phi_{delay}$ (%)[a]	τ_p[b] (ns)	τ_d[b] (μs)	$k_{r,s}$[c] (×10⁷ S⁻¹)	$k_{nr,T}$[c] (×10⁴ S⁻¹)	k_{isc}[d] (×10⁷ S⁻¹)	k_{risc}[d] (×10⁴ S⁻¹)
4SpAc35CzPy	62.0/38.1/23.9	11.3	37.9	3.38	1.62	5.50	2.67
4Ac35CzPy[e]	65.1/11.7/53.4	11.8	73.2	1.0	0.54	7.4	7.0

[a] Total PL quantum yield, prompt FL quantum yield, and delayed FL quantum yield. [b] TrPL decay time: τ_p (prompt luminescence half-life); τ_d (delayed luminescence half-life). [c] Radiative and non-radiative decay. [d] Intersystem crossing rate constant (k_{isc}) and the reverse intersystem crossing rate constant (k_{risc}). [e] See ref. 42.

quenching between the **4SpAc35CzPy** molecules. Indeed, the PLQY increases to 75% (Fig. S9(b), ESI†) in a doped film of **4SpAc35CzPy** (15%) in **o-DiCbzBz**, in agreement with this hypothesis, indicating that the concentration quenching effect in the pristine film is significant.

Electroluminescence performance of 4SpAc35CzPy. To examine **4SpAc35CzPy**, a practical emitter for blue TADF

OLEDs, devices with a configuration of ITO/1,1-bis[[di-4-tolylamino)phenyl]cyclohexane (TAPC)/*N*,*N*-dicarbazolyl-3,5-benzene (mCP)/emitting layer (EML)/diphenylbis[4-(pyridin-3-yl)phenyl]silane (DPPS)/LiF/Al were fabricated and tested. The EML was composed of **4SpAc35CzPy** doped into **o-DiCbzBz**.[45] The device structure, TAPC, mCP, and DPPS are shown in Fig. 6. The literature HOMO and LUMO of TAPC, mCP, and
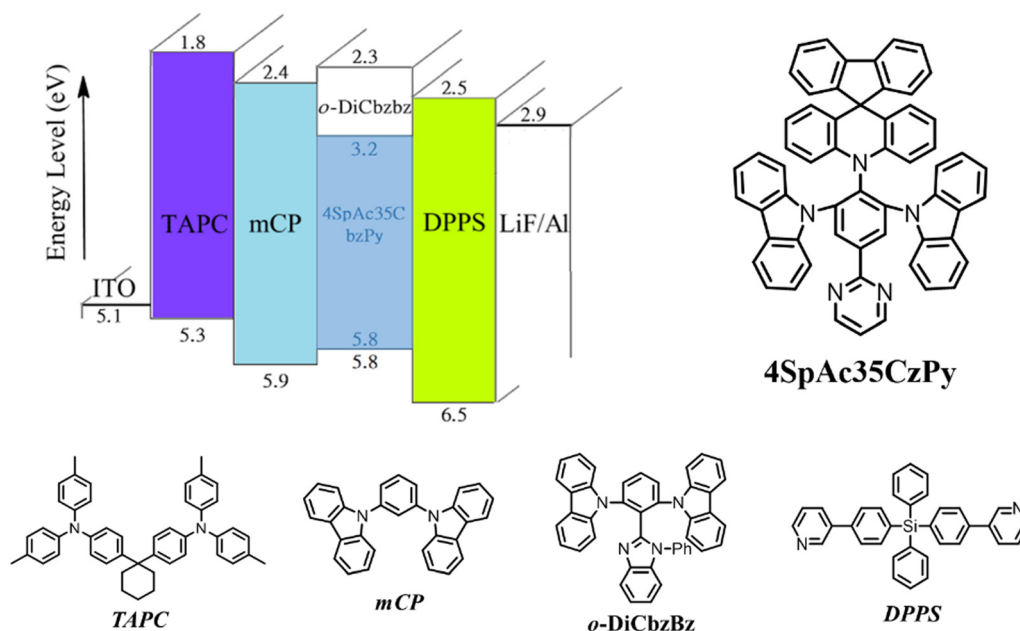

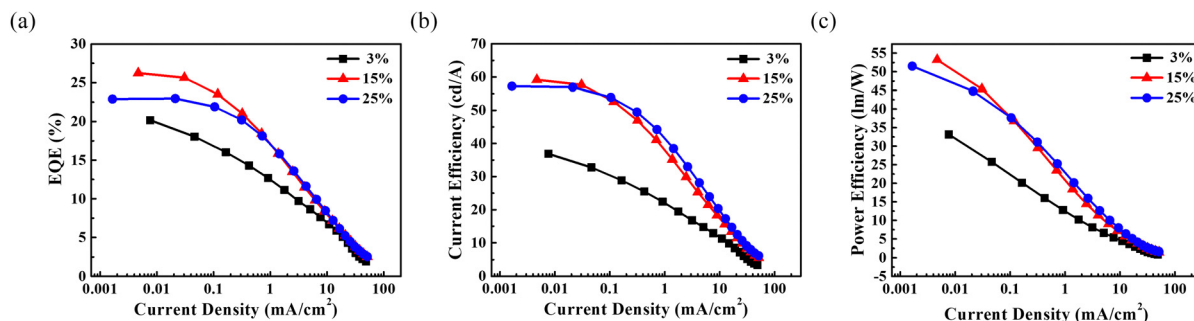Fig. 6 The EL device structure and the HOMO/LUMO levels of the components.

14532 | *J. Mater. Chem. C*, 2025, **13**, 14527–14538

This journal is © The Royal Society of Chemistry 2025

Fig. 7 The TADF OLED's performance was measured using various **4SpAc35CzPy** dopant concentrations in **o-DiCbzBz**.

Table 4 The concentration effects of **4SpAc35CzPy** as a dopant in **o-DiCbzBz**

Doped device	Driving voltage[a] (V)	Turn-on voltage[b] (V)	L_{max} (nits)	η_{EQE} (%)	η_{CE}^{max} (cd A^{-1})	η_{PE}^{max} (lm W^{-1})	$\lambda_{(4V)}^{max}$ (nm)	$\lambda_{(9.5V)}^{max}$ (nm)	CIE@9.5 V
3%	7.87	3.37	1677	20.2	36.9	33.2	484	480	(0.165, 0.274)
15%	8.16	3.33	2851	26.3	59.2	53.2	492	490	(0.179, 0.365)
25%	8.10	3.50	3156	23.0	57.3	51.5	500	497	(0.200, 0.426)

[a] At 10 mA cm^{-2}. [b] At 1 cd m^{-2}.

DPPS are used.[46] TAPC, mCP, and DPPS act as the hole transporting layer (HTL), electron blocking layer (EBL), and electron transporting layer (ETL), respectively. The HOMO of **4SpAc35CzPy** was recorded using an AC-II (Fig. S10, ESI†). The LUMO is estimated from the HOMO and the optical gap E_g.

In the initial screening of the dopant concentration effects, we adopted OLEDs with various concentrations of **4SpAc35CzPy** in **o-DiCbzBz**. The device structures were ITO/TAPC (50 nm)/mCP (10 nm)/**4SpAc35CzPy** (3, 15, and 25%): **o-DiCbzBz** (30 nm)/DPPS (55 nm)/LiF (1.0 nm)/Al (120 nm), and the results are summarized in Fig. 7 and Table 4. Concentration effects are observed on the spectral shift and the device's efficiency. With the EML having 15% **4SpAc35CzPy** doped into **o-DiCbzBz**, the OLED shows the highest η_{EQE} of 26.3% (Fig. 7a), an η_{CE}^{max} of 59.2 cd A^{-1} (Fig. 7b), and an η_{PE}^{max} of 53.2 lm W^{-1} (Fig. 7c). The spectral properties are stable within the applied electrical voltage range of 4–8 V. However, when the doping concentration of **4SpAc35CzPy** increases, the emission λ_{max} gradually shifts from sky-blue to greenish-blue. It is worth mentioning that the OLED shows a high η_{EQE} of 20.2% and a blue emission at a low **4SpAc35CzPy** doping concentration of 3%, with a relatively blue CIE of (0.165,0.274) at 9.5 V (Fig. S11 and Table S2, ESI†).

The performance of the OLED devices was further optimized by tuning the relevant parameters, including the

4SpAc35CzPy-dopant concentration and thicknesses of the HTL, EBL, ETL, and EML (Table 5 and Tables S1 and S2, and Fig. S12, ESI†). When the thickness of the DPPS layer is between 50 and 60 nm, the DPPS thickness effect becomes small, and the η_{EQE}^{max} falls into the range of 26.2 ± 0.4%. These results imply that the charge recombination zone has already fallen into the EML. On the other hand, the thickness of the DPPS would affect the CIE of the OLED. Probably due to the cavity effect, when thickness of the DPPS layer increases, the CIE shifts to the greenish-blue region. The OLED device shows the bluest CIE of (0.178,0.366) at 9.5 V with a luminescence intensity of 2442 cd m^{-2} when the thickness of the DPPS layer is 50 nm.

Fig. 8(a–e) and Table 6 list the spectral and EL properties of the OLEDs, with the EML of 15% doped **4SpAc35CzPy** and the non-doped **4SpAc35CzPy**, and are compared with the literature data of 12% doped **4Ac35CzPy**. The 15% doped **4SpAc35CzPy** OLED has been newly fabricated. The DPPS thickness adopted in the study is normalized to 60 nm for comparison.

The OLED data show good reproducibility; the device achieves the highest current efficiency (η_{CE}^{max}) of 55.7 cd A^{-1}, power efficiency (η_{PE}^{max}) of 50.1 lm W^{-1}, and η_{EQE}^{max} of 26.7%, respectively (Fig. 7a–c). These are much better than those of the OLED with the pristine **4SpAc35CzPy** as the light-emitting layer. By contrast, the **4Ac35CzPy** device shows an η_{CE}^{max} of 53.3 cd A^{-1}, an η_{PE}^{max} of 48.1 lm W^{-1}, and an η_{EQE}^{max} of 21.2%. In addition,

Table 5 DPPS (ETL) thickness effects on the chromatic properties of the OLED with **4SpAc35CzPy** (15%) doped in **o-DiCbzBz** as the emissive layer

ETL thickness (nm)	Driving voltage[a] (V)	Turn-on voltage[b] (V)	L_{max} (nits)	η_{EQE} (%)	η_{CE}^{max} (cd A^{-1})	η_{PE}^{max} (lm W^{-1})	$\lambda_{(4V)}^{max}$ (nm)	$\lambda_{(9.5V)}^{max}$ (nm)	CIE@9.5 V
50	8.47	3.37	3262	25.7	58.7	52.9	492	490	(0.178, 0.366)[c]
55	8.16	3.33	2851	26.3	59.2	53.2	492	490	(0.179, 0.365)[d]
60	8.98	3.43	2627	26.7	55.7	50.1	498	494	(0.195, 0.396)[e]

[a] At 10 mA cm^{-2}. [b] At 1 cd m^{-2}. [c] At 9.5 V (L =2442 cd m^{-2}). [d] At 9.5 V (L = 2398 cd m^{-2}). [e] At 9.5 V (L = 1889 cd m^{-2}).

This journal is © The Royal Society of Chemistry 2025

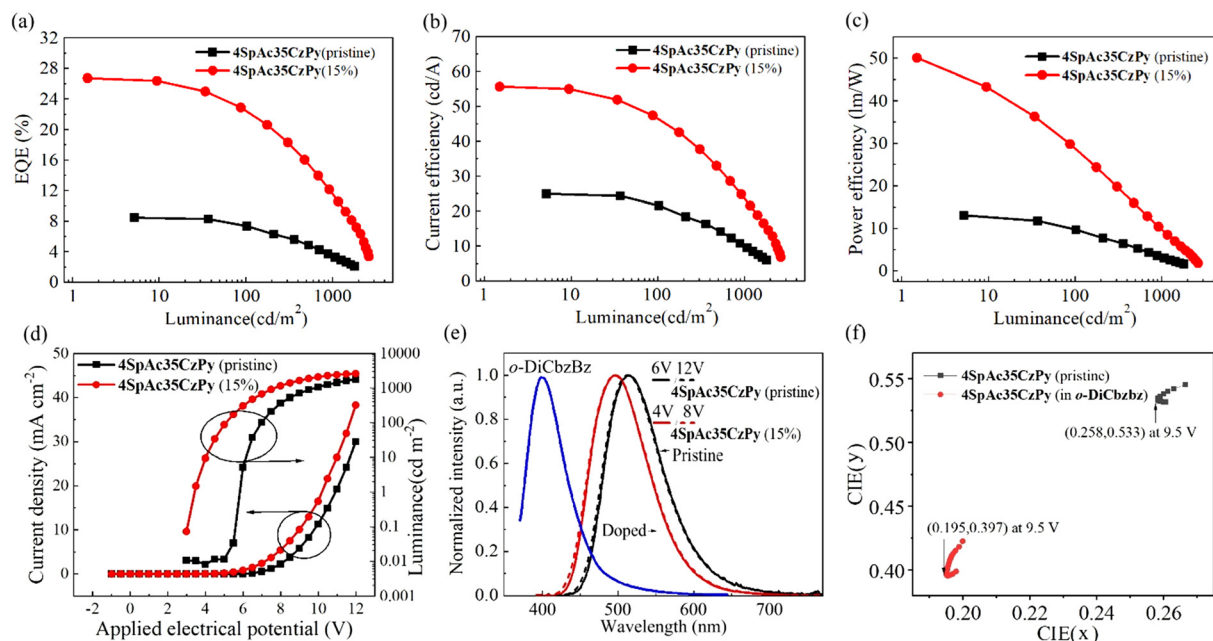J. Mater. Chem. C, 2025, **13**, 14527–14538 | **14533**

Fig. 8 Spectral and EL properties of the OLEDs, using 15% **4SpAc35CzPy** doped or the non-doped **4SpAc35CzPy** as the EML: (a) EQE *vs.* luminescence; (b) CE *vs.* luminescence; (c) PE *vs.* luminescence; (d) current density *vs.* applied electrical potential; (e) EL spectrum; (f) CIE (*x,y*).

Table 6 EL properties of the OLEDs, with the EML of 15% doped **4SpAc35CzPy** and the non-doped **4SpAc35CzPy**

Light emitting layer	V_{on}^{a} (V)	L^{b} (cd m^{-2})	η_{CE}^{c} (cd A^{-1})	η_{PE}^{c} (lm W^{-1})	η_{EQE}^{c} (%)	λ_{EL} (nm)	CIE^{d} (*x,y*)
4SpAc35CbzPy (15%)^{e}	3.4	2627	55.7/47.2/23.8	50.1/29.1/9.8	26.7/22.6/11.6	498	(0.195, 0.396)
4SpAc35CbzPy (pristine)	5.8	1804	24.9/21.7/10.0	13.1/9.78/3.22	8.46/7.39/3.45	514	(0.258, 0.533)
4Ac35CzPy (12%)^{f}	3.4	2724	53.3/44.9/31.1	48.1/32.9/14.9	21.2/17.2/11.9	494	(0.185, 0.403)

^{a} Turn-on voltage at 1 cd m^{-2}. ^{b} Maximum luminance. ^{c} Measured at the maximum, 100 cd m^{-2} and 1000 cd m^{-2}. ^{d} Measured at 9.5 V with L = 891 cd m^{-2}. ^{e} The 15% doped **4SpAc35CzPy** OLED fabrication has been reproduced. The adopted thickness of DPPS is 60 nm. The CIE (*x,y*) was collected at 9.5 V with L = 1889 cd m^{-2}. ^{f} The thickness of DPPS is 55 nm.

these devices still demonstrate reasonable efficiency at a high luminance of 100 cd m^{-2} with an η_{EQE} of 22.6%, which is still higher than the η_{EQE}^{max} of the **4Ac35CzPy** device. However, the η_{EQE} roll-off was significant at high brightness; an η_{EQE}^{max} of 11.6% was recorded at 1000 cd m^{-2}. A similar η_{EQE}^{max} of 11.9% was recorded for the OLED of **4Ac35CzPy**; the efficiency roll-off can be rationalized by triplet–triplet annihilation (TTA) and triplet-polaron annihilation (TPA) quenching mechanisms, which is a common phenomenon in TADF OLEDs. The lifetime of **4SpAc35CzPy** is shown in Fig. S13 and Table S3 (ESI†).

The doped device has a lower turn-on voltage (V_{on}) of 3.4 V at 1 cd m^{-2} than the pristine one, a higher current can be injected, as demonstrated in the *J*–*V* plots (Fig. 7(d)), so that the 15% **4SpAc35CzPy** doped OLED achieves the highest luminance of 2627 cd m^{-2}. Fig. 7(e) shows the EL emissive spectra peaked at 498 nm and 514 nm for the 15% **4SpAc35CzPy** doped and pristine **4SpAc35CzPy** emitting layers, respectively, corresponding to the Commission Internationale de l'éclairage (CIE) 1931 coordinates of (0.195,0.396) and (0.258,0.533), respectively. The 15% **4SpAc35CzPy** doped device is bluer than the pristine one.

The TADF phenomenon was finally evidenced by observing the delayed luminescence in the transient electroluminescence experiments. Fig. 9 shows the delayed luminescence after cutting off the electrical power supply. The half-life of the luminescence decay is slightly shorter when the driving current density is higher. This is consistent with the assumption of the diffusive bimolecular TPA and TPQ quenching mechanisms; under a higher driving current density, a high triplet exciton concentration is expected to be generated in the charge recombination zone, which may lead to stronger TPA and TPQ quenching effects. Applying reverse electrical voltage biases does not alter the decay half-life, indicating that the delayed luminescence is not due to the recombination of the excessive charges in the light-emitting matrix.

To understand more deeply the photo and electroluminescence behavior of **4Ac35CzPy** and **4SpAc35CzPy**, NTO analysis was performed using Gaussian 16. Although NTO analysis does not provide a full evaluation of the vibronic interactions and dynamics of the internal conversion and intersystem crossing behavior of the excited molecules,[47] the NTO approach leads to a preliminary and intuitive picture of the orbitals involved in a hole-particle excitation, allowing one to understand the related
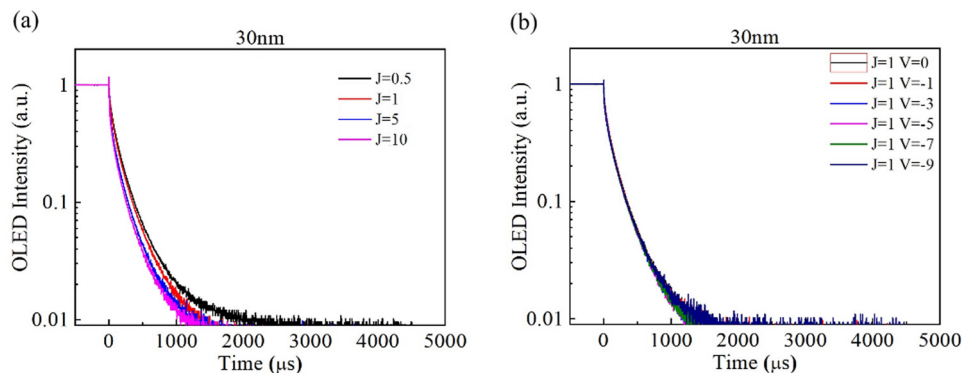
Fig. 9 The transient electroluminescence of the 15% **4SpAc35CzPy**: **o-DiCbzBz** TADF–OLED. Delayed luminescence was observed after cutting off the power supply: (a) TrEL with different driving currents. (b) TrEL with different reverse-bias electrical voltages.

photophysical properties qualitatively.[48] The relevant NTO calculations are presented in Fig. S14–S17 and Tables S4 and S5 (ESI†).

Since the TADF pathways involve RISC, the mechanisms should obey quantum mechanical guidelines: (1) for transitions between two excited states, the states should be coupled according to the Frank–Condon principle; the most probable transitions between electronic excited states should be alike, suggesting that the initial state wave function (ψ(i)) most closely resembles that of the final state (ψ(f)). The energy and momentum should be conserved between states ψ(i) and ψ(f).[49] (2) According to the hybridized local-and-charge-transfer (HLCT) excited state theory, when an excited state possesses a charge transfer (CT) and a locally-excited (LE) excited state
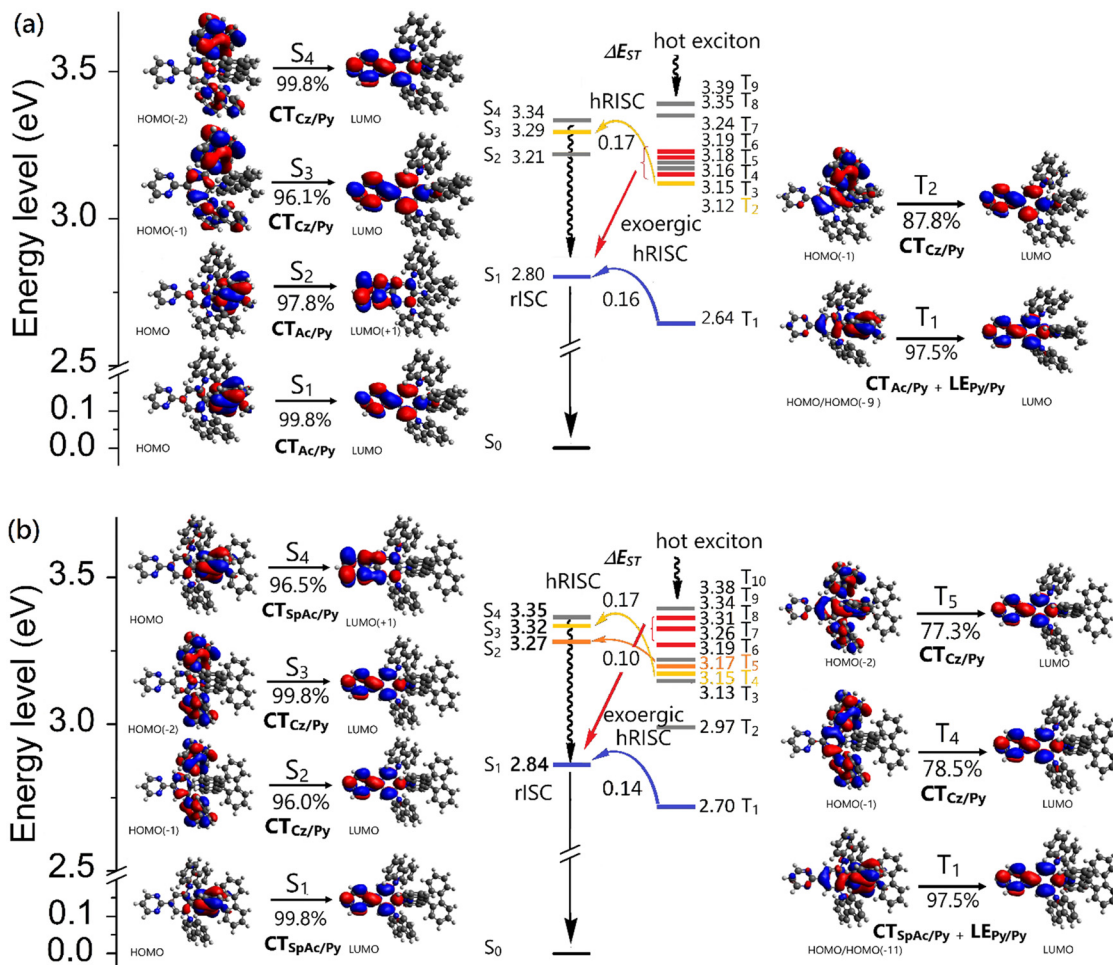

Fig. 10 Natural transition orbital analysis of (a) **4Ac35CzPy** and (b) **4SpAc35CzPy**.

components, a high-lying reversed intersystem crossing (hRISC) may occur; while the CT component assists the hRISC process for fast and effective triplet utilization in OLEDs, the LE component secures adequate PLQY.[50] The hRISC process that occurs from the upper levels of triplet states (T_n, $n \geq 2$)[51] is also called the "hot exciton" mechanism,[52] which provides channels to achieve a fast and exergonic RISC process. However, to realize the "hot exciton" mechanisms, some prerequisite conditions must be matched: (i) a large energy gap (ΔE_T) between T_n and T_{n-1} is required to suppress the decay of T_n through internal conversion. Usually, an ΔE_T larger than 0.5 eV is assumed.[53] (ii) A singlet excited state (S_m) lying slightly below the T_n state with an appreciable SOC between S_m and T_n to allow the intersystem crossing to facilitate, and (iii) the T_n energy should be reasonably low and is not formed by electric injection.

Some common features for both **4Ac35CzPy** and **4SpAc35CzPy** are summarized according to our NTO analyses, shown in Fig. 10. These features might explain the high blue TADF OLED performance of **4Ac35CzPy** and **4SpAc35CzPy**.

(i) CT from the acridan HOMO to the phenylenepyrimidine LUMO has a significant contribution to the S_1 states of **4Ac35CzPy** and **4SpAc35CzPy**. A reasonable HOMO/LUMO overlap allows this CT state to be luminescent; even though the LE component of the central phenylene ring is relatively minor, interactions between the acridan and phenylenepyrimidine moieties allow the S_1 state to fluoresce with a PLQY of 0.6–0.7, either in solutions or in films.

(ii) Their T_1 states are an HLCT state. The T_1 state also arises mainly from the CT of acridan (HOMO) to the phenylenepyrimidine (LUMO), but mixed with a few percent contribution from the LE (π–$\pi^\star$) state of the phenylenepyrimidine group. This provides moderate spin–orbit coupling between the S_1 and T_1 states (Tables S4 and S5). Furthermore, the small ΔE_{ST} values of $\sim$0.14–0.15 eV, would allow the rISC to proceed.

(iii) The hRISC of hot excitons may proceed within the OLED devices. For **4Ac35CzPy**, the calculated ΔE_T (T_2–T_1) between the T_2 and T_1 states is 0.48 eV. The gap is large, and the T_2 to T_1 internal conversion might be slow, giving a chance for hRISC to compete. For **4SpAc35CzPy**, although an additional T_2 state corresponding to the LE of the fluorenyl group is found, the T_2 is spatially separated from T_3 and T_1. Therefore, slow relaxation from T_3 to T_1 through T_2 is expected. Furthermore, the ΔE_T (T_3–T_1) of 0.43 eV is large; direct internal conversion from T_3 to T_1 would also be slow. In addition, the spin–orbit coupling values between T_2 and S_m, are small. We believe that the T_2 state may not be involved in the hRISC.

(iv) Introduction of the carbazole units at the 3- and 5-positions leads to manifold triplets and singlets at nearly degenerated energy levels, within a range of 0.2 eV. This would enhance the probability of multichannel hRISC from T_n to S_m,[54] among which some transitions labelled yellow have a small ΔE_{ST} of 0.17 eV and with relatively large SOC values (Fig. S22, ESI†). The occurrence of hRISC between these states cannot be excluded.

(v) Some triplet states, labelled in red, have a large SOC with S_1. Even though the ΔE_{ST} between the T_m ($m < 10$) and S_1 is

around 0.4 eV, a large SOC may still allow the exoergic RISC to occur.

However, introducing a spirofluorenyl group to **4SpAc35CzPy** does lead to several changes and differences. First, as mentioned before, the S_2(CT) state of **4SpAc35CzPy** is derived from the carbazole to the phenylenepyrimidine group, which is different from the S_2(CT) state of **4Ac35CzPy** derived from the acridan to the phenylene–pyrimidine units. In addition, in **4SpAc35CzPy**, the T_2 state is involved in a LE of the spirofluorenyl, and the overlap integrals between T_m(CT) and T_2(LE) are small. Therefore, the internal conversion from T_3–T_6 to T_2 should be slow. This would allow the hRISC from T_3–T_6 to the S_2 state to compete. In particular, the small energy differences among T_3–T_6 would allow them to couple with each other, and the SOC for T_5(CT, Cz/Py) to S_2(CT, Cz/Py) of **4SpAc35CzPy** is large. This would provide an extra opportunity for hRISC. Finally, the spirofluorenyl group may suppress the energy loss caused by intramolecular vibrations, reducing the radiationless decay and further optimizing the TADF characteristics. This hypothesis is consistent with the long lifetime in the TrEL in Fig. 9. All these may contribute to the superior TADF OLED performance of **4SpAc35CzPy**.

Conclusion

With appropriate design, we have successfully designed **4SpAc35CzPy**, a D–A type acridan-pyrimidine TADF emitter that shows a high EQE in the sky-blue emission region. Consistent with the previously reported results,[21,40,55,56] adopting a spiroacridan moiety as the electron-donating substituent leads to higher performance in TADF OLEDs. The light-emitting devices show improved sky-blue emission with an η_{EQE}^{max} of 26% and a CIE of (0.178, 0.366) at a brightness of 2442 cd m^{-2}.

Data availability

The data that support the findings of this study are available from the corresponding author, Man-kit Leung, upon reasonable request.

Conflicts of interest

There are no conflicts to declare.

Acknowledgements

14536 | *J. Mater. Chem. C*, 2025, **13**, 14527–14538

This journal is © The Royal Society of Chemistry 2025

spectrometry technical research services from the Consortia of Key Technologies, National Taiwan University.

References

1 Q.-y Meng, H.-y Shao, R. Wang, C.-y Yao, Y.-l Wang, X.-l Wen, J.-y Xu, Y. Dai and J. Qiao, *Adv. Mater.*, 2024, **36**, 2407882.

2 D. Hall, J. C. Sancho-García, A. Pershin, D. Beljonne, E. Zysman-Colman and Y. Olivier, *J. Phys. Chem. A*, 2023, **127**, 4743–4757.

3 X. Mu, D. Li, D. Liu, J. Wang, J. Li, C. Liu, J. Zhang, T. Feng, K. Fang, W. Li and Z. Ge, *Adv. Opt. Mater.*, 2024, **12**, 2401735.

4 C. Si, T. Wang, Y. Xu, D. Lin, D. Sun and E. Zysman-Colman, *Nat. Commun.*, 2024, **15**, 7439.

5 X. Chen, S. Bagnich, R. Pollice, B. Li, Y. Zhu, R. Saxena, Y. Yin, W. Zhu, A. Aspuru-Guzik, E. Zysman-Colman, A. Köhler and Y. Wang, *Adv. Opt. Mater.*, 2024, **12**, 2301784.

6 M. Y. Wong and E. Zysman-Colman, *Adv. Mater.*, 2017, **29**, 1605444.

7 H. Uoyama, K. Goushi, K. Shizu, H. Nomura and C. Adachi, *Nature*, 2012, **492**, 234–238.

8 S. Diesing, L. Zhang, E. Zysman-Colman and I. D. W. Samuel, *Nature*, 2024, **627**, 747–753.

9 Z. Xiao, Y. Zou, X. Song, N. Li, J. Miao, K. Li, C. Yang and X. Peng, *Chem. Eng. J.*, 2024, **482**, 149150.

10 H. Lim, H. J. Cheon, S.-J. Woo, S.-K. Kwon, Y.-H. Kim and J.-J. Kim, *Adv. Mater.*, 2020, **32**, 2004083.

11 B. S. Kim and J. Y. Lee, *Adv. Funct. Mater.*, 2014, **24**, 3970–3977.

12 U. Shakeel and J. Singh, *Org. Electron.*, 2018, **59**, 121–124.

13 L. G. Franca, A. Danos and A. Monkman, *J. Mater. Chem. C*, 2022, **10**, 1313–1325.

14 S. Izumi, H. F. Higginbotham, A. Nyga, P. Stachelek, N. Tohnai, P. d Silva, P. Data, Y. Takeda and S. Minakata, *J. Am. Chem. Soc.*, 2020, **142**, 1482–1491.

15 X. Song, S. Shen, S. Zou, Y. Wang, F. Guo, S. Gao and Y. Zhang, *Chem. Eng. J.*, 2024, **481**, 148794.

16 R. Komatsu, H. Sasabe, Y. Seino, K. Nakao and J. Kido, *J. Mater. Chem. C*, 2016, **4**, 2274–2278.

17 I. S. Park, S. Y. Lee, C. Adachi and T. Yasuda, *Adv. Funct. Mater.*, 2016, **26**, 1813–1821.

18 K. Wu, T. Zhang, L. Zhan, C. Zhong, S. Gong, N. Jiang, Z.-H. Lu and C. Yang, *Chem. – Eur. J.*, 2016, **22**, 10860–10866.

19 L. Yu, Z. Wu, G. Xie, W. Zeng, D. Ma and C. Yang, *Chem. Sci.*, 2018, **9**, 1385–1391.

20 R. Gavale, M. Ghasemi, F. Khan, D. Volyniuk, J. V. Grazulevicius and R. Misra, *J. Mater. Chem. C*, 2024, **12**, 2134–2147.

21 Y. Huang, M. Jia, C. Li, Y. Yang, Y. He, Y. Luo, Y. Huang, L. Zhou and Z. Lu, *Chem. Commun.*, 2024, **60**, 3194–3197.

22 A. Khan, W. Qiang, S. Kumar, T. Leydecker and Z. Wang, *Dyes Pigm.*, 2025, **232**, 112478.

23 H.-Z. Li, F.-M. Xie, K. Zhang, Y. Shen, W. Zhou, Y.-Q. Li, W.-J. Wang and J.-X. Tang, *Chem. Eng. J.*, 2022, **436**, 135234.

24 Y. H. Lee, W. Lee, T. Lee, J. Jung, S. Yoo and M. H. Lee, *Chem. Eng. J.*, 2023, **452**, 139387.

25 F.-E. Szu, S.-A. Chen, Y.-Y. Yu, J.-H. Lee, T.-L. Chiu and M.-K. Leung, *J. Mater. Chem. C*, 2024, **12**, 15112–15118.

26 I. S. Park, H. Komiyama and T. Yasuda, *Chem. Sci.*, 2017, **8**, 953–960.

27 R. Komatsu, T. Ohsawa, H. Sasabe, K. Nakao, Y. Hayasaka and J. Kido, *ACS Appl. Mater. Interfaces*, 2017, **9**, 4742–4749.

28 B. Li, Z. Li, X. Song, F. Guo, Y. Wang, S. Gao and Y. Zhang, *Dyes Pigm.*, 2022, **203**, 110373.

29 U. Tsiko, D. Volyniuk, V. Andruleviciene, K. Leitonas, G. Sych, O. Bezvikonnyi, V. Jasinskas, V. Gulbinas, P. Stakhira and J. V. Grazulevicius, *Mater. Today Chem.*, 2022, **25**, 100955.

30 T. Serevičius, J. Dodonova, R. Skaisgiris, D. Banevičius, K. Kazlauskas, S. Juršėnas and S. Tumkevičius, *J. Mater. Chem. C*, 2020, **8**, 11192–11200.

31 F. Rodella, R. Saxena, S. Bagnich, D. Banevičius, G. Kreiza, S. Athanasopoulos, S. Juršėnas, K. Kazlauskas, A. Köhler and P. Strohriegl, *J. Mater. Chem. C*, 2021, **9**, 17471–17482.

32 R. Komatsu, H. Sasabe and J. Kido, *J. Photonics Energy*, 2018, **8**, 032108.

33 G. Meng, X. Chen, X. Wang, N. Wang, T. Peng and S. Wang, *Adv. Opt. Mater.*, 2019, **7**, 1900130.

34 J. Pandidurai, J. Jayakumar, Y.-K. Chen, C.-M. Hsieh and C.-H. Cheng, *J. Mater. Chem. C*, 2021, **9**, 15900–15909.

35 H. Xia, Y. Tang, Y. Zhang, F. Ni, Y. Qiu, C.-W. Huang, C.-C. Wu and C. Yang, *J. Mater. Chem. C*, 2022, **10**, 4614–4619.

36 P. Ganesan, D.-G. Chen, J.-L. Liao, W.-C. Li, Y.-N. Lai, D. Luo, C.-H. Chang, C.-L. Ko, W.-Y. Hung, S.-W. Liu, G.-H. Lee, P.-T. Chou and Y. Chi, *J. Mater. Chem. C*, 2018, **6**, 10088–10100.

37 H.-N. Shi, F.-M. Xie, H.-Z. Li, Y.-Q. Li and J.-X. Tang, *J. Mater. Chem. C*, 2025, **13**, 5582–5590.

38 Y. Jiang, J. Jin, H. Ren, B. Liu, Y. Mei, M. Xu, D. Liu and J. Li, *Chem. – Eur. J.*, 2024, **30**, e202401250.

39 H. Guo, Z. Tang, L. Gong, R. Tang, S. Yang, W. Yu, Y. Liu, H. Wang, O. Ablikim, B. Qu, J. Wei, Z. Chen and L. Xiao, *Adv. Opt. Mater.*, 2024, **12**, 2401832.

40 T.-A. Lin, T. Chatterjee, W.-L. Tsai, W.-K. Lee, M.-J. Wu, M. Jiao, K.-C. Pan, C.-L. Yi, C.-L. Chung, K.-T. Wong and C.-C. Wu, *Adv. Mater.*, 2016, **28**, 6976–6983.

41 Y.-K. Chen, J. Jayakumar, C.-L. Ko, W.-Y. Hung, T.-L. Wu and C.-H. Cheng, *J. Mater. Chem. C*, 2022, **10**, 9241–9248.

42 Y.-Z. Li, H.-C. Liang, C.-H. Chen, C.-H. Chiu, B.-Y. Lin, J. A. Tan, J.-H. Lee, T.-L. Chiu and M.-k Leung, *J. Mater. Chem. C*, 2023, **11**, 14395–14403.

43 K. N. Blodgett, D. Sun, J. L. Fischer, E. L. Sibert and T. S. Zwier, *Phys. Chem. Chem. Phys.*, 2019, **21**, 21355–21369.

44 N. Manfredi, C. Decavoli, C. L. Boldrini, C. Coluccini and A. Abbotto, *Energies*, 2020, **13**, 3937.

45 J.-J. Huang, Y.-H. Hung, P.-L. Ting, Y.-N. Tsai, H.-J. Gao, T.-L. Chiu, J.-H. Lee, C.-L. Chen, P.-T. Chou and M.-k Leung, *Org. Lett.*, 2016, **18**, 672–675.

46 B.-Y. Lin, Y.-R. Li, C.-H. Chen, H.-C. Hsu, M.-K. Wei, J.-H. Lee and T.-L. Chiu, *Opt. Express*, 2022, **30**, 18066–18078.

This journal is © The Royal Society of Chemistry 2025

J. Mater. Chem. C, 2025, **13**, 14527–14538 | **14537**

47 S. Mai and L. González, *Angew. Chem., Int. Ed.*, 2020, **59**, 16832–16846.

48 J.-H. Li, J.-D. Chai, G. Y. Guo and M. Hayashi, *Chem. Phys. Lett.*, 2011, **514**, 362–367.

49 N. J. Turro, V. Ramamurthy and J. C. Scaiano, *Modern molecular photochemistry of organic molecules*, University Science Books, Sausalito, CA, 2010.

50 S. Xiao, Y. Gao, R. Wang, H. Liu, W. Li, C. Zhou, S. Xue, S.-T. Zhang, B. Yang and Y. Ma, *Chem. Eng. J.*, 2022, **440**, 135911.

51 R. Keller, *Chem. Phys. Lett.*, 1969, **3**, 27–29.

52 R. Wang, T. Hu, Y. Liu, X. Wei, J. Liu, Z. Li, X. Hu, H. Gao, G. Liu and Y. Yamada-Takamura, *J. Phys. Chem. C*, 2020, **124**, 20816–20826.

53 Y. Zhu, S. Vela, H. Meng, C. Corminboeuf and M. Fumanal, *Adv. Opt. Mater.*, 2022, **10**, 2200509.

54 H. Qi, H. Huang, S. He, S. Wang, L. Peng, Y. Liu, S. Xue, D. Ma, S. Ying and S. Yan, *ACS Mater. Lett.*, 2025, **7**, 1019–1027.

55 H. Peng, Y. Xu, C. Zhou, R. Pei, J. Miao, H. Liu and C. Yang, *Adv. Funct. Mater.*, 2023, **33**, 2211696.

56 Y.-K. Qu, Q. Zheng, J. Fan, L.-S. Liao and Z.-Q. Jiang, *Acc. Mater. Res.*, 2021, **2**, 1261–1271.

14538 | *J. Mater. Chem. C*, 2025, **13**, 14527–14538

This journal is © The Royal Society of Chemistry 2025